RSC Advances

PAPER

View Article Online
View Journal | View Issue



Cite this: *RSC Adv.*, 2017, **7**, 24683

# Enhanced photocatalytic removal of NO over titania/hydroxyapatite ($TiO_2$/HAp) composites with improved adsorption and charge mobility ability†

Jie Yao,[ab] Yufei Zhang,[b] Yawen Wang,*[a] Meijuan Chen,[c] Yu Huang,*[b] Junji Cao,[b] Wingkei Ho[d] and Shun Cheng Lee[e]

Effective photocatalysis processes with production of fewer toxic intermediates are highly desirable for air purification. In this study, titania/hydroxyapatite ($TiO_2$/HAp) composites were synthesized by a facile hydrothermal method and employed to decontaminate nitric oxide (NO) in air under simulated solar light irradiation for the first time. It was found that the photocatalytic activity of the as-prepared $TiO_2$/HAp composite (44.61%) was superior to those of the pristine components ($TiO_2$: 38.57%, HAp: 36.73%) and mechanically mixed samples (35.36%). The $TiO_2$/HAp composite with mass ratio of 3 : 1 (75% $TiO_2$/HAp) exhibited the highest NO removal efficiency among them. Moreover, the toxic intermediate $NO_2$ production was significantly inhibited over $TiO_2$/HAp. These synergistically improved properties can be ascribed to the high separation efficiency and faster transfer of the photo-generated charge carriers as evidenced by the experimental results from photocurrent tests and electrochemical impedance spectroscopy (EIS). The results from temperature programmed desorption (TPD) confirmed that the 75% $TiO_2$/HAp sample had stronger chemisorption for NO due to the increased concentration of surface OH groups. Furthermore, the electron spin resonance (ESR) characterization suggested that $^{\bullet}O_2^-$ and $^{\bullet}OH$ radicals were the major species involved for NO removal over $TiO_2$/HAp composites. The five recycling tests suggested that the $TiO_2$/HAp has superior photocatalytic stability. This study suggests that the combination of $TiO_2$ with HAp is an effective approach for air purification.

Received 21st February 2017
Accepted 1st May 2017

DOI: 10.1039/c7ra02157g

rsc.li/rsc-advances



## 1. Introduction

Nitric oxides ($NO_x$) generated from the combustion of fossil fuels have attracted lots of attention because they can lead to various environmental problems, such as acid rain, haze, photochemical smog, ozone depletion and destruction of animal and plant species.[1] The control of $NO_x$ in the atmosphere has become one of the greatest challenges in environmental protection. Several techniques have been developed for removing $NO_x$, such as electrochemical methods,[2] a chemical absorption-biological reduction integrated system,[3] selective catalytic reduction[4] and semiconductor photocatalysis.[5] Among these methods, semiconductor photocatalysis is a promising technology for low concentration air purification, because it allows for the utilization of renewable, safe and clean solar light to solve environmental problems.

Titanium dioxide ($TiO_2$) is one of the most popular photocatalysts in view of its non-toxicity, cheapness and excellent photochemical stability. However, the drawbacks of low adsorption capacity for pollutants[6,7] and high recombination of photogenerated electron–hole pairs[8,9] impair its photocatalytic performance. In order to solve these issues, several strategies have been adopted to enhance the photocatalytic efficiency. For example, modification with noble metals on the surface of $TiO_2$ is considered as an efficient way for improving the photocatalytic activity.[10,11] Besides, the combination of $TiO_2$ with other semiconductor materials of suitable band structure (*e.g.* $C_3N_4$, $Ag_2CO_3$, $Fe_2O_3$, and $Bi_2WO_6$, *etc.*) can improve the charge separation efficiency and prolong the life of charges, enhancing the photocatalytic activity of $TiO_2$ eventually.[12–14] However, the above two strategies can not solve the drawback of low adsorption capacity for pollutants. Recently, some literatures reported that $TiO_2$ supported materials, such as zeolite, silica, purity natural diatomite (rich in $SiO_2$ 87–91%), activated carbon, hydroxyapatite (HAp), can offer abundant active adsorption sites, which resulted in quick mass transfer and fast catalytic reactions.[15–19]

[a]College of Chemistry and Chemical Engineering, Taiyuan University of Technology, Taiyuan 030024, China. E-mail: wangyawen@tyut.edu.cn

[b]Key Lab of Aerosol Chemistry & Physics, Institute of Earth Environment, Chinese Academy of Sciences, Xi'an 710061, China

[c]School of Human Settlements and Civil Engineering, Xi'an jiaotong University, Xi'an 710049, China

[d]Department of Science and Environmental Studies, The Education University of Hong Kong, Hong Kong, China

[e]Department of Civil and Environmental Engineering, The Hong Kong Polytechnic University, Hung Hom, Hong Kong, China

† Electronic supplementary information (ESI) available. See DOI: 10.1039/c7ra02157g

Among these supported materials, hydroxyapatite (HAp), $Ca_{10}(PO_4)_6(OH)_2$, with mechanical stability, non-toxicity, good biocompatibility, and low cost has been widely studied. Yuichi Komazaki *et al.* reported that $NO_2$ was effectively collected on HAp in the annular diffusion scrubber.[21] Due to its inherent hexagonal crystal, HAp possess hydroxyl ions ($OH^-$) channels, which can enhance the electrical conductivity and charge carrier migration.[20] The surface OH groups or $H_2O$ molecules adsorbed can react with the $h^+$ to produce hydroxyl ($^{\bullet}OH$) radicals. Fu *et al.* reported that the $ZnSn(OH)_6$ provided a mass of OH groups and facilitated $^{\bullet}OH$ radicals formation to enhance the photocatalytic performance.[22] In addition, the electron state change of the $PO_4^{3-}$ groups in the surface of HAp during the photocatalytic process can result in the generation of $^{\bullet}O_2^-$ radicals.[23] Dai *et al.* also found that the oxygen vacancies were formed on the surface of HAp and acted as electrons receiver to achieve the electron–hole pairs separation.[24]

Hence, it is expected that combining the merits of HAp with $TiO_2$ can not only improve the adsorption capacity of $TiO_2$ for pollutants, but also decrease the recombination of photo-generated electron–hole pairs. So the combination of $TiO_2$ and HAp may be an effective approach for air purification. In this paper, the $TiO_2$/HAp composites were synthesized by a hydrothermal method. The as-prepared $TiO_2$/HAp composites showed excellent photocatalytic activity on $NO_x$ removal under the simulated solar light. The physical and chemical properties of the $TiO_2$/HAp were deeply discussed and the possible photocatalytic mechanism was proposed.

## 2. Experimental section

### 2.1. Materials

Titanium tetrachloride ($TiCl_4$, analytical pure), ammonium hydroxide solution ($NH_3 \cdot H_2O$ solution, 25%–28wt%, analytical pure), ammonium phosphate ($(NH_4)_2HPO_4$, analytical pure), calcium nitrate ($Ca(NO_3)_2 \cdot 4H_2O$, analytical pure), absolute ethyl alcohol ($C_2H_6O$, analytical grade) were purchased from Sinopharm (Shanghai, China) and used without further treatment.

### 2.2. Sample synthesis

The $TiO_2$/HAp composites were prepared by adding a certain amount of as-prepared $TiO_2$ powder into the precursor solution of HAp through a facile hydrothermal treatment. Firstly, 18 mL $NH_3 \cdot H_2O$ solution (25%–28 wt%) was added dropwise into 10 mL $TiCl_4$ solution and simultaneously stirred for 2 hour. Next, the white precipitate was collected by centrifugal separation, and washed thoroughly with deionized water and absolute ethyl alcohol for several times, and then dried at 60 °C overnight. The precursor powder was dispersed in 60 mL deionized water with vigorously stirring. Then it was put in 100 mL Teflon-lined autoclave and kept at 190 °C for 8 h to obtain the $TiO_2$ powder. Secondly, $(NH_4)_2HPO_4$ and $Ca(NO_3)_2$ were dissolved in water with a molar ratio of Ca/P = 1.67. Then its pH value was adjusted by ammonia to 9–10. The prepared $TiO_2$ powder was added into the above solution and stirred for 2 h to get a suspension. Next, the suspension was transferred into a Teflon-lined autoclave and subsequently heated at 190 °C for 8 h. The obtained products were centrifuged and washed with deionized water and absolute ethyl alcohol, and then dried at 60 °C overnight.

To get $TiO_2$/HAp composites with different mass ratios, the amount of $TiO_2$ powder was varied. The samples with mass ratios of $TiO_2$ : HAp = 1 : 1, 3 : 1, 5 : 1 were labeled as 50%, 75% and 83% $TiO_2$/HAp (calculating by the ratio of $TiO_2$), respectively. For comparison, the pure HAp was prepared under the same procedure without adding $TiO_2$ powder.

### 2.3. Characterization

The XRD patterns were collected on a Philips X'pert PRO SUPER diffractometer using Cu K$\alpha$ radiation ($\lambda$ = 1.5406 Å) at a scan rate of 0.05° 2$\theta$ per s. FTIR (Magna-IR 50, Nicolet, America) spectra was obtained using a Fourier transform infrared spectroscopy absorption spectrometer from 4000 to 400 $cm^{-1}$ at room temperature. X-ray photoelectron spectroscopy (XPS) were collected on ThermoFisher Scientific photoelectron spectrometer (Escalab 250Xi). The morphologies of as-prepared samples were analyzed by transmission electron microscopy (TEM, JEM-2010, Japan), and high-resolution transmission electron microscopy (HRTEM) microscopy. The specific surface areas of the as-synthesized samples were determined by $N_2$ sorption using a Micromeritics Gemini 2390 analyzer and the pore size distribution was calculated using the Barrett–Joyner–Halenda (BJH) model. UV-vis diffuse reflectance spectra (DRS) was recorded by a UV-vis spectrophotometer using $BaSO_4$ as the reference standard. Temperature programmed desorption (TPD) was carried out on a chemisorption analyzer (BJbuilder, PCA 1200, China). The sample for electron spin resonance spectroscopy (ER200-SRC, BRUKER, Germany) was prepared by mixing 0.05 prepared samples in a 25 mM DMPO solution with 50 mL aqueous dispersion for DMPO-$^{\bullet}OH$ or 50 mL alcohol dispersion for DMPO-$^{\bullet}O_2^-$, respectively. The light irradiation source was a 300 W Xe arc lamp (PLS-SXE 300, Beijing).

### 2.4. Evaluation of photoelectrochemical properties

The photoelectrochemical properties of pure $TiO_2$, HAp and $TiO_2$/HAp composites were carried out using a Parstat 4000 electrochemical workstation (USA) in a conventional three-electrode cell. In this three-electrode cell system, Ag/AgCl electrode and a platinum plate were used as reference electrode and counter electrode, respectively. In order to fabricate the working electrode, 0.09 wt% ethyl cellulose and 0.73 wt% terpineol were dissolved in ethanol, then 0.18 wt% sample was added in the above solution to obtain homogeneous suspension by bath sonication. Then the samples were coated on the fluorine doped tin oxide (FTO) glass through dip coating method. In order to remove the additives, the prepared electrodes were heat-treated in a furnace at 500 °C for 30 min. The current–time curves were measured at 0.2 V *vs.* Ag/AgCl in 0.1 mol $L^{-1}$ $Na_2SO_3$ solution under a 300 W Xe arc lamp irradiation. Electrochemical impedance spectroscopy (EIS) was analyzed at a frequency range of 0.1 Hz to 100 kHz with a 5 mV voltage amplitude under

 

open-circuit voltage in 1 mmol $L^{-1}$ $K_3Fe(CN)_6$ and $K_4Fe(CN)_6$ solution.

### 2.5. Evaluation of photocatalytic activity

The photocatalytic activity of the as-synthesized samples was investigated through the removal of NO at ppb level in a continuous flow reactor (30 cm × 15 cm × 10 cm) under simulated solar light irradiation at room temperature. The dispersed photocatalyst (0.1 g) was coated on a glass dish ($D$ = 9.0 cm) (as shown in Fig. S1†). Then the dishes were treated at 70 °C until complete removal of water in the suspension. The simulated solar light source was a commercial 300 W Xe arc lamp (PLS-SXE 300, Beijing), which was vertical placed 20 cm above the reactor. The light intensity at the surface of the as-synthesized samples was controlled at 0.75 W $cm^{-2}$ as measured by a photometer (THORLABS PD130, USA). The NO gas at ppb level was obtained from a compressed gas cylinder at a concentration of 50 ppm of NO ($N_2$ balance). The 50 ppm of NO was diluted to about 420 ppb by the air stream from a zero air generator. The flow rate of the gas streams was controlled at 3 L $min^{-1}$ by a mass flow controller. The lamp was not turned on until the adsorption–desorption equilibrium among catalysts, gases and water vapor was obtained. The concentration of NO, $NO_2$, and $NO_x$ was continuously measured every 1 minute by a $NO_x$ analyzer (Ecotech, 9841) at a sampling rate of 0.6 L $min^{-1}$. The removal ratio ($R$) of NO after irradiation was calculated according to the following equation:

$$R\ (\%) = (1 - C/C_0) \times 100\%$$

where $C$ is the outlet concentration of NO each access gases, and $C_0$ is the inlet concentration before irradiation.

## 3. Results and discussion

### 3.1. Phase structure and chemical composition

Fig. 1a show the XRD patterns of $TiO_2$, HAp and $TiO_2$/HAp composites. For the pure $TiO_2$, the diffraction peaks at 25.2°, 37.8°, 48.0°, 53.9°, 55.2°, 62.7°, 68.5°, 70.3° are consistent with the characteristic peaks of anatase-$TiO_2$ (JCPDS, 04-0477).[25] As for pure HAp, all diffraction peaks and their relative intensities are agreement with the standard power diffraction patterns of hexagonal phase HAp (JCPDS, 09-0432). Fig. 1b shows the crystal structure model of HAp. It is clearly seen that the hydroxyapatite surface is rich in $OH^-$ groups, $PO_4^{3-}$ groups. No other impurity peak is observed, which indicates that pure $TiO_2$ and HAp are successfully synthesized. Moreover, the diffraction patterns of the other three samples (50%, 75% and 83% $TiO_2$/HAp composites) show that both anatase-$TiO_2$ and hexagonal phase HAp are existed. It can be concluded that the $TiO_2$/HAp composites were successfully synthesized by the hydrothermal method. Obviously, the intensities of $TiO_2$ diffraction peaks have corresponding positive relationship with its relative content in the composites (50%, 75% and 83% $TiO_2$/HAp).

The FTIR spectra of pure $TiO_2$, HAp and $TiO_2$/HAp composites are shown in Fig. 1c. The peaks at 3429 and 1626 $cm^{-1}$ are caused by the lattice water of samples.[26] The typical broad absorption bands of $TiO_2$ are observed at 800–450 $cm^{-1}$, which is attributed to the stretching vibration of Ti–O–Ti bonds.[27] For HAp sample, the characteristic bands of $PO_4^{3-}$ present at 472 $cm^{-1}$ ($\nu_2$), 562 and 604 $cm^{-1}$ ($\nu_4$), 966 $cm^{-1}$ ($\nu_1$) and 1031 and 1095 $cm^{-1}$($\nu_3$).[28] The peaks appearing at 3573 and 633 $cm^{-1}$ are attributed to stretching and bending vibration modes of OH bands of HAp, respectively.[29] For the $TiO_2$/HAp composites, well-preserved characteristic peaks of $TiO_2$ and HAp in the spectra of $TiO_2$/HAp (50%, 75% and 83%) composites, indicating no change of structure or phase transformation of $TiO_2$ and HAp after composites synthesis. This observation demonstrates that the $TiO_2$/HAp composites are synthesized successfully, which is consistent with the XRD results.

XPS was used to further determine surface chemical composition and chemical states of pure $TiO_2$, HAp and $TiO_2$/HAp composites. Fig. 2 shows the XPS spectra of $TiO_2$, HAp and 75% $TiO_2$/HAp. In Fig. 2a Ti, O, Ca and P elements are observed in the survey spectra of $TiO_2$/HAp. The additional C element peak is mainly derived from the adventitious carbon as shown in Fig. 2b, the Ti 2p peaks of $TiO_2$ located at 459.2 eV and 464.7 eV are attributed to the Ti–O bonds.[30] However, the Ti 2p peaks of 75% $TiO_2$/HAp move to 458.7 eV and 464.3 eV respectively, the lower energy levels, which could result from the existence of the Ti–O–Ca bonds in $TiO_2$/HAp. Similarly, Duo

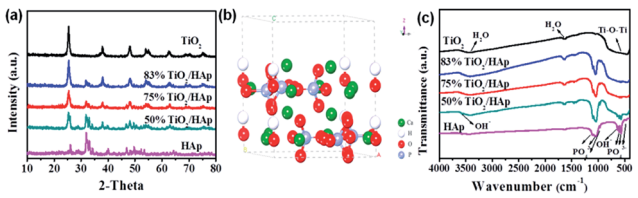


Fig. 1 XRD patterns of as-synthesized samples (a), the crystal structure models of HAp (b) and FTIR spectra of $TiO_2$, HAp and $TiO_2$/HAp (50%, 75% and 83%) composites (c).

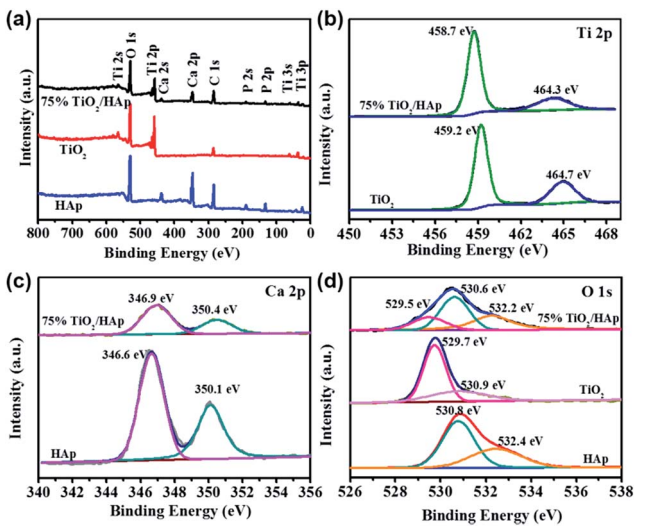


Fig. 2 Survey XPS spectra (a) and high-resolution XPS spectra of Ti 2p (b), Ca 2p (c), and O 1s (d) of the as-prepared samples.

*et al.* reported that the shift of the Ti 2p peaks in the $TiO_2$/BiOCl composite was ascribed to the formation of Ti–O–Bi bonds.[31] In Fig. 2c the Ca 2p peaks of HAp located at 346.6 eV and 350.1 eV are observed, while the Ca 2p peaks of 75% $TiO_2$/HAp shift to 346.9 eV and 350.4 eV.[32] Fig. 2d shows the corresponding high-resolution O 1s spectra of pure $TiO_2$, HAp and $TiO_2$/HAp. The two peaks at 529.7 eV and 530.9 eV in $TiO_2$ are assigned to the Ti–O bonds and –OH groups, respectively.[33] The two peaks at 530.8 eV and 532.4 eV in HAp are attributed to phosphate group ($PO_4^{3-}$) and adsorbed water, respectively.[34] The three peaks at 529.5 eV, 530.6 eV and 532.2 eV in 75% $TiO_2$/HAp are assigned to lattice oxygen species $TiO_2$ (Ti–O bonds), phosphate group ($PO_4^{3-}$) and chemically adsorbed oxygen species of water, respectively.[34]

### 3.2. Morphological analysis

The microcomposition and crystal structure of $TiO_2$, HAp and $TiO_2$/HAp were further analysed by TEM microscopy. Fig. 3a shows that the as-prepared $TiO_2$ contains of intersection nanoparticles with an irregular shape. The size range of $TiO_2$ is from 11 nm to 39 nm. In Fig. 3b the HAp power is composed of rod-like nanocrystals with the length of 32.17–127.23 nm and the width of 14.96–40.49 nm. Fig. 3c shows the TEM image of 75% $TiO_2$/HAp composite. It is clearly seen that 75% $TiO_2$/HAp possesses both irregular $TiO_2$ nanoparticles and rod-like HAp. In particular, the size of HAp in 75% $TiO_2$/HAp is the length of 63.40–49.32 nm and width of 19.51–15.73 nm, smaller as compared to pure HAp. The size change is probably ascribed to the addition of $TiO_2$ precursor powers, which inhibits the growth of HAp. Miao Xu and coworker also reported that the addition of g-$C_3N_4$ can efficiently decrease the particle size of $Ag_2O$ in the g-$C_3N_4$/$Ag_2O$ composite preparation process.[35]

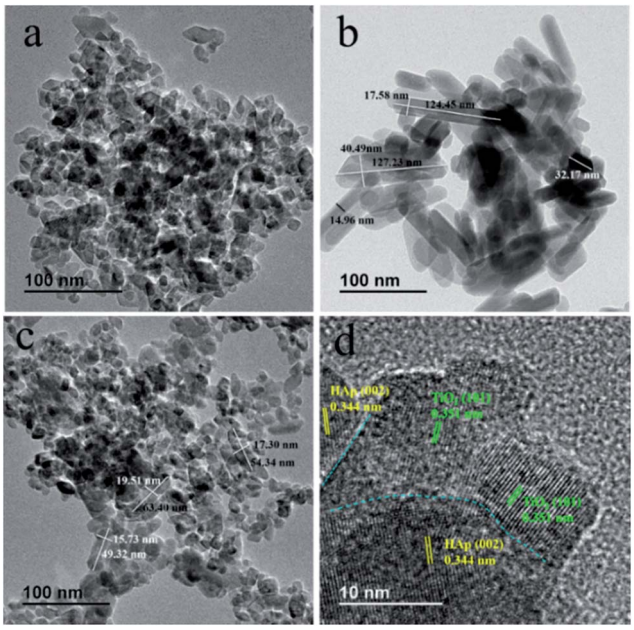


Fig. 3 TEM images of pure $TiO_2$ (a), HAp (b), 75% $TiO_2$/HAp composite (c), and HRTEM images for 75% $TiO_2$/HAp composite (d).

Fig. 3d shows the HRTEM image of the 75% $TiO_2$/HAp. The lattice spacing of approximately 0.351 and 0.344 nm is ascribed to the (101) crystal plane of anatase-$TiO_2$ nanoparticles (JCPDS, 04-0477) and the (002) crystal plane of rod-like hexagonal phase HAp (JCPDS, 09-0432), respectively. The distinct intersections of lattice fringes are observed in Fig. 3d, indicating an intimate contact is formed between $TiO_2$ and HAp.

The $N_2$ adsorption–desorption isotherms and pore size distributions of samples are presented in Fig. S2.† The specific surface areas and average pore diameters of pure $TiO_2$, HAp and $TiO_2$/HAp composites are shown in Table 1. The BET specific surface areas of pure $TiO_2$, HAp, 83% $TiO_2$/HAp, 75% $TiO_2$/HAp, 50% $TiO_2$/HAp and are 73, 54, 98, 80 and 57 $m^2\ g^{-1}$, respectively. The BET specific surface areas of except 50% $TiO_2$/HAp are much higher than that of the pure $TiO_2$ and HAp. It indicates that except 50% $TiO_2$/HAp has the better photocatalytic activity, this may be due to the existence of a mass of surface active sites.[36]

### 3.3. Photocatalytic activity and stability

The photocatalytic degradation NO in air of the as-prepared samples is investigated. Fig. 4a shows the NO concentration *vs.* irradiation time curves of $TiO_2$/HAp composites, mechanically mixed $TiO_2$/HAp (mass ratios of $TiO_2$ and HAp = 3 : 1, the same ratio to 75% $TiO_2$/HAp composite), pure $TiO_2$ and HAp under solar light irradiation. All $TiO_2$/HAp (50%, 75% and 83%) composites show better NO removal performance as compared to pure $TiO_2$ and HAp. The NO removal ratio of 75% $TiO_2$/HAp is the highest of 44.61% among the six samples. In order to make a clearly quantitative comparison, we used the Langmuir–Hinshelwood model in the initial time period to evaluate the rates of NO photodegradation. According to previous study,[37] the linear plot between $\ln(C_0/C)$ and irradiation time ($t$) indicates that photocatalytic NO degradation over the as-prepared samples follows first-order order kinetics. The rate constant ($k_{NO}$) for $TiO_2$, HAp, and $TiO_2$/HAp composites are listed in Fig. 4b. The $k_{NO}$ (0.1462 $min^{-1}$) of 75% $TiO_2$/HAp is the highest among the samples. The $k_{NO}$ follows the order of 75% $TiO_2$/HAp > 83% $TiO_2$/HAp > 50% $TiO_2$/HAp > $TiO_2$ > HAp, which is different from the BET result, and their specific surface area follows the order of 83% $TiO_2$/HAp > 75% $TiO_2$/HAp > $TiO_2$ > 50% $TiO_2$/HAp > HAp. It indicates that the specific surface area is not the only reason accounting for the improved photocatalytic activity. The NO removal activity and reaction rate constants ($k_{NO}$) over the 75% $TiO_2$/HAp composite with and without light irradiation were shown in Fig. S3 and Table S2,† respectively. It's clear to see that the 75% $TiO_2$/HAp composite shows excellent photocatalytic activity on NO removal, while the

Table 1 Summary of surface area, and pore diameter of the pure and composite materials

| Sample | $TiO_2$ | 83% $TiO_2$/HAp | 75% $TiO_2$/HAp | 50% $TiO_2$/HAp | HAp |
|---|---|---|---|---|---|
| $S_{BET}$ ($m^2\ g^{-1}$) | 73 | 98 | 80 | 57 | 54 |
| Pore diameter (nm) | 12.9 | 11.2 | 14.9 | 30.5 | 39.9 |

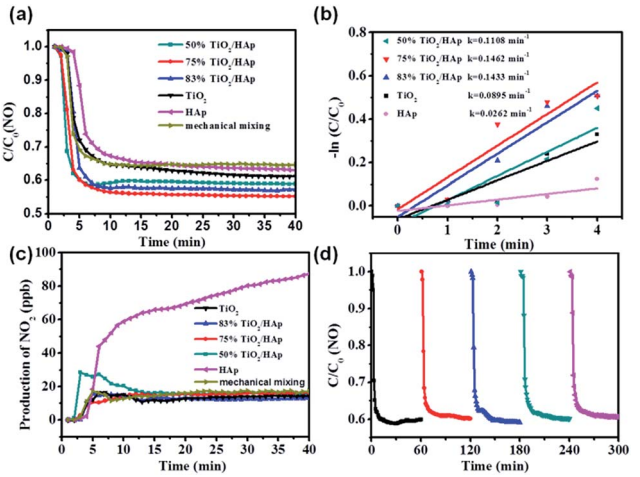


Fig. 4 (a) The solar light photocatalytic activity of pure $TiO_2$, HAp, $TiO_2$/HAp composite and mechanical mixing (mass ratios of $TiO_2$ and HAp = 3 : 1) for the removal of NO in air; (b) reaction rate constants $k$; (c) production of $NO_2$ and (d) recycling property of 75% $TiO_2$/HAp sample under simulated solar light irradiation for the removal of NO.

activity without light irradiation was ignorable. Furthermore, the NO removal ratio of the $TiO_2$/HAp sample as-prepared through the mechanically mixed method is 35.36% under the same condition, which is lower than that of 75% $TiO_2$/HAp. Therefore, 75% $TiO_2$/HAp composite has better photocatalytic activity than simply mixing, indicating that the interfacial contact between $TiO_2$ and HAp in the composite benefits the photocatalytic performance.

In addition, the toxic intermediate $NO_2$ generation is monitored simultaneously in the NO photocatalytic oxidation process. Fig. 4c shows that the amount of $NO_2$ produced by $TiO_2$ and $TiO_2$/HAp (50%, 75% and 83%) composites was about 12.1–15.8 ppb, much lower than that of 87.5 ppb produced by HAp. It indicates that the addition of $TiO_2$ is beneficial to inhibit the generation of $NO_2$. The above results demonstrate that 75% $TiO_2$/HAp shows the best photocatalytic activity.

The photocatalytic stability of 75% $TiO_2$/HAp composite was evaluated. In Fig. 4d, the removal ratio of NO in the five cycle experiments was not significantly decreased, the maximum of 44.61% and the minimum of 41.02%. It suggests that the $TiO_2$/HAp composites possess favorable stability and durability property.

### 3.4. Mechanism of photocatalytic activity improvement

Generally, the improved photocatalytic activity of catalysts is related to their optical absorption ability, target pollutant-catalyst adsorption/desorption ability, and the charge carriers' mobility. Fig. 5a shows the UV-vis diffuse reflectance spectroscopy to investigate the optical properties of the samples. The optical absorption edges and band gap energies ($E_g$) for the as-prepared samples are shown in Table S1.† It clear seen that the absorption edge of pure $TiO_2$ is located at 413 nm, corresponding to band gap ($E_g$) of 3.01 eV, while the absorption edge of pure HAp is less than 250 nm. Compared with pure HAp, the

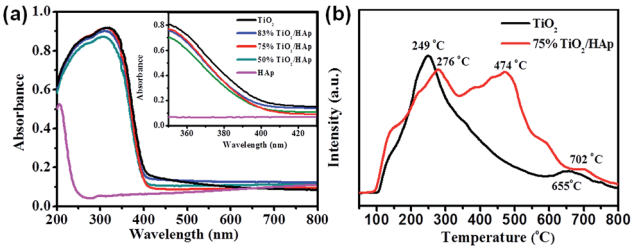


Fig. 5 (a) UV-vis DRS spectra of pure $TiO_2$, HAp, $TiO_2$/HAp composite (inset is magnification spectra in the range of 300–500 nm), (b) TPD profiles of NO for pure $TiO_2$ and 75% $TiO_2$/HAp composite.

absorption edge of the $TiO_2$/HAp composites shows a significant red shift. Moreover, the absorption edge of the $TiO_2$/HAp composites shows a slight blue shift compare with $TiO_2$, which indicates that the $TiO_2$/HAp composites possess higher oxidation capacity than pure $TiO_2$.

In order to investigate the adsorption/desorption process of NO on the synthesized photocatalysts, temperature programmed desorption (TPD) tests were carried out. Fig. 5b shows that in the TPD curves of pure $TiO_2$, there appear two desorption peaks located at around 249 °C and 655 °C, which were assigned to the desorption of NO and $NO_2$–$O_2$, respectively. While the 75% $TiO_2$/HAp composite have three main peaks located at around 276 °C, 474 °C and 702 °C. Among them, the stronger desorption peak of NO at 474 °C was assigned to the stronger chemisorption bond between NO and surface OH groups of HAp.[21]

Photocurrent response was employed to investigate the separation efficiency of photo-generated electrons and holes. Fig. 6a shows the photocurrent–time curves of $TiO_2$, HAp and $TiO_2$/HAp composites under the simulated solar light irradiation. There is no photocurrent over pure HAp.[24] The photocurrent density of 75% $TiO_2$/HAp composites is 1.2 times as high as the pure $TiO_2$, which indicates that more efficient separation of the photo-generated electron–hole pairs over 75% $TiO_2$/HAp. According to the TEM and XPS results, the transfer and separation of the photo-generated carriers relate to the intimate interfacial contact between $TiO_2$ and HAp, which improves photocatalytic activity of the $TiO_2$/HAp.

Moreover, in order to explain the interfacial charge transfer and charge carriers recombination, electrochemical impedance

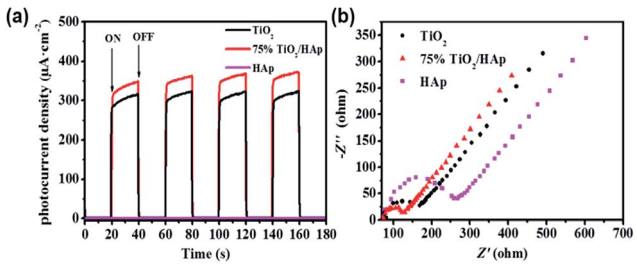


Fig. 6 Transient photocurrent densities (a) and electrochemical impedance spectroscopy measurements (b) of pure $TiO_2$, HAp, $TiO_2$/HAp composite.

spectroscopy (EIS) measurements of pure $TiO_2$, HAp and 75% $TiO_2$/HAp composite were carried out in dark. The arc in the Nyquist plot can reflect the charge transfer process, and the semicircle diameter semicircle represents the charge transfer resistance.[38] Fig. 6b shows that 75% $TiO_2$/HAp composite has the smallest diameter of arc in Nyquist plot comparing with pure $TiO_2$ and HAp, which indicates that 75% $TiO_2$/HAp improve electron migration and promote the separation of photo-generated carriers.

In order to further reveal the photocatalytic mechanism of $TiO_2$/HAp composite, ESR was investigated to determine the active reaction groups. As shown in Fig. 7, the characteristic peaks of the DMPO-$^{\bullet}O_2^-$ adducts (originated form $^{\bullet}O_2^-$ radicals) are observed from HAp, while signals of DMPO-$^{\bullet}$OH (four characteristic peaks of DMPO-$^{\bullet}$OH with an intensity ratio of 1 : 2 : 2 : 1 originated form $^{\bullet}$OH radicals) adducts are weak, which is conformity with previous study.[39] For pure $TiO_2$, the appearance of DMPO-$^{\bullet}$OH and the absence of DMPO-$^{\bullet}O_2^-$ signal indicate that NO is removed through oxidation by $^{\bullet}$OH radicals *via* pure $TiO_2$. The band positions of $TiO_2$ can be theoretically calculated by the following equations:[40] $E_{VB} = \chi - E^e + 0.5\ E_g$, $E_{CB} = E_{VB} - E_g$, where $E_{VB}$ is the valance band edge potential, $E_{CB}$ is conduction band edge potential, $\chi$ represents the electronegativity of the semiconductor, which is the geometric mean of the electronegativity of the constituent atoms, where the $\chi$ of $TiO_2$ calculated to be 5.81 eV. $E^e$ is the energy of free electrons on the hydrogen scale (~4.5 eV),[41,42] $E_g$ is the band gap energy of the semiconductor, which is calculated from the results of UV-vis diffuse reflectance spectroscopy. The VB and CB potentials of pure $TiO_2$ are calculated to be 2.81 eV and −0.20 eV, respectively. Because the CB potential of $TiO_2$ is more positive than the redox potential of $O_2/^{\bullet}O_2^-$ (−0.33 eV),[43] the $^{\bullet}O_2^-$ radicals could not be formed, which is consistent with the ESR results. The VB of $TiO_2$ is more positive than that of OH/$^{\bullet}$OH (1.99 eV),[44] thus the photo-generated hole can oxidize OH into $^{\bullet}$OH radicals. The signal intensity of $^{\bullet}$OH radicals in 75% $TiO_2$/HAp is significant stronger than that in pure $TiO_2$ and HAp, which demonstrates that the combination of $TiO_2$ and HAp can promote the generation of $^{\bullet}$OH radicals. Additionally, 75% $TiO_2$/HAp have similar signal intensity of $^{\bullet}O_2^-$ radicals to HAp, while it is significant stronger than that in pure $TiO_2$. It may be because the electron state change of the $PO_4^{3-}$ groups in the surface of HAp in photocatalytic process under UV irradiation can result in the generation of $^{\bullet}O_2^-$ radicals.[5,23,45]

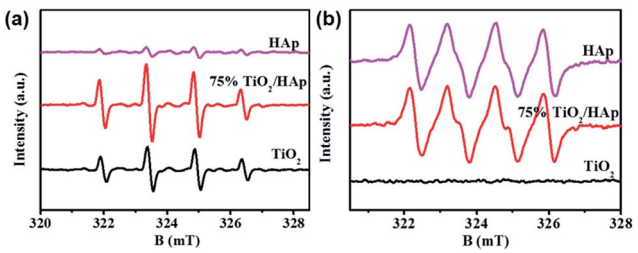


Fig. 7 Electron spin resonance (ESR) spectra of radical adducts trapped for pure $TiO_2$, HAp and 75% $TiO_2$/HAp composite by (a) DMPO-$^{\bullet}$OH and (b) DMPO-$^{\bullet}O_2^-$ under simulated solar-light irradiation.

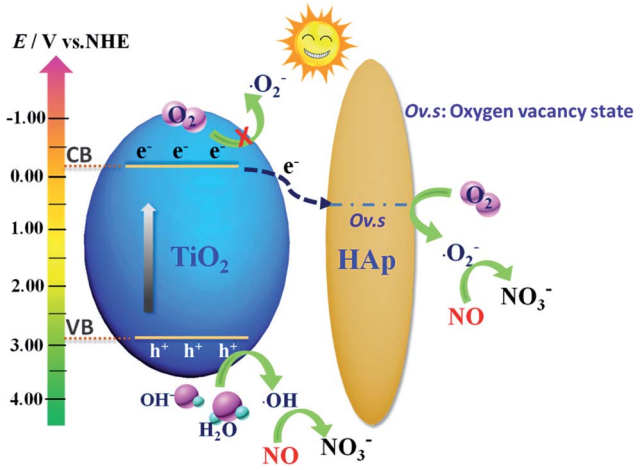


Fig. 8 Photocatalytic mechanism scheme of $TiO_2$/HAp under simulated solar light irradiation.

Based on the above analysis, the photocatalytic mechanism of $TiO_2$/HAp composite under simulated solar light irradiation is showed in Fig. 8. $TiO_2$ photocatalyst is excited by the simulated solar light irradiation to generate photoinduced electrons which are then transferred to the oxygen defect level from the electron state change of the $PO_4^{3-}$ groups in the surface of HAp.[23] Then the electron captured by HAp reacts with the surrounding oxygen on the vacancies to form $^{\bullet}O_2^-$ radicals.[45] Next, a fraction of $^{\bullet}O_2^-$ reacts with $H_2O$ and $H^+$ to form $H_2O_2$, and then the electrons combines with $H_2O_2$ to produce $^{\bullet}$OH radicals.[5] This transfer behavior of the electrons from $TiO_2$ transfer to the vacancy on HAp enhances the separation and lengthens the lifetime of carriers, and inhibits the recombination of photo-generated electrons–holes pairs, and result in the generation of more $^{\bullet}$OH radicals. Simultaneously, the photoinduced hole on the VB of $TiO_2$ reacts with $H_2O$ or $OH^-$ to form $^{\bullet}$OH radicals. At last, the $^{\bullet}O_2^-$ and $^{\bullet}$OH radicals can further react with $NO_x$ to produce $NO_3^-$.

## 4. Conclusion

In summary, $TiO_2$/HAp composite has been successfully synthesized by a facile hydrothermal method. The NO removal ratio of 75% $TiO_2$/HAp is 44.61%, which is the highest among the pure $TiO_2$, HAp and $TiO_2$/HAp composites. The results of TPD analysis, photocurrent generation and EIS measurements demonstrated that the enhanced photocatalytic activity of $TiO_2$/HAp composites can be ascribed to stronger chemisorption for NO, higher separation efficiency and faster transfer of the photo-generated electron–holes pairs. The ESR results revealed that $^{\bullet}O_2^-$ and $^{\bullet}$OH radicals as the major active species in the photocatalytic reaction process. The photocatalytic removal mechanism of NO over the $TiO_2$/HAp composites is illustrated in detail. This study suggests that 75% $TiO_2$/HAp composites with the highest photocatalytic activity is considered to be a promising air-cleaning material.

## Acknowledgements

This research was financially supported by the National Science Foundation of China (41573138, 41401567), the Key Project of International Cooperation of the Chinese Academy of Sciences (GJHZ1543). Yu Huang is also supported by the "Hundred Talent Program" of the Chinese Academy of Sciences.

## Notes and references

1 Y. J. Sun, Z. W. Zhao, F. Dong and W. Zhang, *Phys. Chem. Chem. Phys.*, 2015, **17**, 10380–10390.
2 Q. Guo, Y. He, T. Sun, Y. Wang and J. Jia, *J. Hazard. Mater.*, 2014, **276**, 371–376.
3 Y. F. Xia, B. H. Lu, N. Liu, Q. L. Chen, S. J. Li and W. Li, *Bioresour. Technol.*, 2013, **149**, 184–190.
4 Z. Liu, Y. Yi, S. Zhang, T. Zhu, J. Zhu and J. Wang, *Catal. Today*, 2013, **216**, 76–81.
5 Y. Huang, Y. Gao, Q. Zhang, J. J. Cao, R. J. Huang, W. Ho and S. C. Lee, *Appl. Catal., A*, 2016, **515**, 170–178.
6 T. S. Natarajan, J. Y. Lee, H. C. Bajaj, W. K. Jo and R. J. Tayade, *Catal. Today*, 2016, **282**, 13–23.
7 Y. Liu, C. Y. Liu, J. H. Wei, R. Xiong, C. X. Pan and J. Shi, *Appl. Surf. Sci.*, 2010, **256**, 6390–6394.
8 H. Liu, T. Lv, C. Zhu and Z. Zhu, *Sol. Energy Mater. Sol. Cells*, 2016, **153**, 1–8.
9 D. Friedmann, C. Mendive and D. Bahnemann, *Appl. Catal., B*, 2010, **99**, 398–406.
10 H. Wang, J. L. Faria, S. Dong and Y. Chang, *Mater. Sci. Eng., B*, 2012, **177**, 913–919.
11 Q. Lu, Z. Lu, Y. Lu, L. Lv, Y. Ning, H. Yu, Y. Hou and Y. Yin, *Nano Lett.*, 2013, **13**, 5698–5702.
12 J. Balbuena, G. Carraro, M. Cruz, A. Gasparotto, C. Maccato, A. Pastor, C. Sada, D. Barreca and L. Sánchez, *RSC Adv.*, 2016, **6**, 74878–74885.
13 N. Mohaghegh, B. Eshaghi, E. Rahimi and M. R. Gholami, *J. Mol. Catal. A: Chem.*, 2015, **406**, 152–158.
14 J. Zhang, L. Huang, L. Yang, Z. Lu, X. Wang, G. Xu, E. Zhang, H. Wang, Z. Kong, J. Xi and Z. Ji, *J. Alloys Compd.*, 2016, **676**, 37–45.
15 M. Gar Alalm, A. Tawfik and S. Ookawara, *J. Environ. Chem. Eng.*, 2016, **4**, 1929–1937.
16 M. R. Eskandarian, M. Fazli, M. H. Rasoulifard and H. Choi, *Appl. Catal., B*, 2016, **183**, 407–416.
17 J. Matos, J. Laine and J. M. Herrmann, *J. Catal.*, 2001, **200**, 10–20.
18 S. K. Padmanabhan, S. Pal, E. Ul Haq and A. Licciulli, *Appl. Catal., A*, 2014, **485**, 157–162.
19 A. Pal, T. K. Jana and K. Chatterjee, *Mater. Res. Bull.*, 2016, **76**, 353–357.
20 M. Buchi Suresh, P. Biswas, V. Mahender and R. Johnson, *Mater. Sci. Eng., C*, 2017, **70**, 364–370.
21 Y. Komazaki, H. Shimizu and S. Tanaka, *Atmos. Environ.*, 1999, **33**, 4363–4371.
22 X. Fu, J. Wang, D. Huang, S. Meng, Z. Zhang, L. Li, T. Miao and S. Chen, *ACS Catal.*, 2016, **6**, 957–968.
23 H. Nishikawa, *J. Mol. Catal. A: Chem.*, 2003, **206**, 331–338.
24 Y. Chai, J. Ding, L. Wang, Q. Liu, J. Ren and W. L. Dai, *Appl. Catal., B*, 2015, **179**, 29–36.
25 L. S. Birks and H. Friedman, *J. Appl. Phys.*, 1946, **17**, 687.
26 Q. Xu, J. Feng, L. Li, Q. Xiao and J. Wang, *J. Alloys Compd.*, 2015, **641**, 110–118.
27 G. Sheng, L. Qiao and Y. Mou, *J. Environ. Eng.*, 2011, **137**, 611–616.
28 N. Pramanik, S. Mohapatra, P. Bhargava and P. Pramanik, *Mater. Sci. Eng., C*, 2009, **29**, 228–236.
29 R. M. Tripathi, N. Kumar, A. Singh Bhadwal, R. K. Gupta, B. R. Shrivastav and A. Shrivastav, *Mater. Lett.*, 2015, **140**, 64–67.
30 W. Li, Y. Tian, H. Li, C. Zhao, B. Zhang, H. Zhang, W. Geng and Q. Zhang, *Appl. Catal., A*, 2016, **516**, 81–89.
31 F. Duo, Y. Wang, C. Fan, X. Mao, X. Zhang, Y. Wang and J. Liu, *Mater. Charact.*, 2015, **99**, 8–16.
32 S. Abbasi, M. R. Bayati, F. Golestani-Fard, H. R. Rezaei, H. R. Zargar, F. Samanipour and V. Shoaei-Rad, *Appl. Surf. Sci.*, 2011, **257**, 5944–5949.
33 K. Li, S. Gao, Q. Wang, H. Xu, Z. Wang, B. Huang, Y. Dai and J. Lu, *ACS Appl. Mater. Interfaces*, 2015, **7**, 9023–9030.
34 M. Salarian, W. Z. Xu, Z. Wang, T. K. Sham and P. A. Charpentier, *ACS Appl. Mater. Interfaces*, 2014, **6**, 16918–16931.
35 M. Xu, L. Han and S. Dong, *ACS Appl. Mater. Interfaces*, 2013, **5**, 12533–12540.
36 H. Y. Zhu, R. Jiang, Y. Q. Fu, R.-R. Li, J. Yao and S. T. Jiang, *Appl. Surf. Sci.*, 2016, **369**, 1–10.
37 Z. Wang, Y. Huang, W. Ho, J. Cao, Z. Shen and S. C. Lee, *Appl. Catal., B*, 2016, **199**, 123–133.
38 W. Teng, X. Li, Q. Zhao and G. Chen, *J. Mater. Chem. A*, 2013, **1**, 9060.
39 H. Nishikawa and K. Omamiuda, *J. Mol. Catal. A: Chem.*, 2002, **179**, 193–200.
40 Q. Wang, D. Jiao, J. Lian, Q. Ma, J. Yu, H. Huang, J. Zhong and J. Li, *J. Alloys Compd.*, 2015, **649**, 474–482.
41 T. B. Li, G. Chen, C. Zhou, Z. Y. Shen, R. C. Jin and J. X. Sun, *Dalton Trans.*, 2011, **40**, 6751–6758.
42 F. Dong, Y. Sun, M. Fu, Z. Wu and S. C. Lee, *J. Hazard. Mater.*, 2012, **219–220**, 26–34.
43 W. Liu, M. Wang, C. Xu, S. Chen and X. Fu, *Mater. Res. Bull.*, 2013, **48**, 106–113.
44 G. Li, D. Q. Zhang, J. C. Yu and M. K. H. Leung, *Environ. Sci. Technol.*, 2010, **44**, 4276–4281.
45 M. Reddy, A. Venugopal and M. Subrahmanyam, *Appl. Catal., B*, 2007, **69**, 164–170.